

MESHFREE FRAMEWORK FOR IMAGE-DERIVED MODELLING

Heye Zhang*, Linwei Wang[†], Peter J Hunter*, Pengcheng Shi[†]

*Bioengineering Institute, University of Auckland, New Zealand

[†]College of Computing and Information Sciences, Rochester Institute of Technology, USA

ABSTRACT

Disorder of electrical propagation pattern might lead to serious heart attacks, so a variety of efforts have been developed to identify pathological patterns. Among those works, the most promising attempt is 3D model-based imaging of cardiac electrical activities. However, current models are computationally expensive and often too complicated to be adopted into clinical data. In this paper, we propose a meshfree framework, which can build a computational model from the image-derived geometry straightforwardly, without burden mesh generation. This image-derived framework opens great possibilities, including the ability to be directly integrated into our previous cardiac information recovery framework or explore cardiac electrical activities with clinical data. Experiments have been conducted on synthetic data to show the ability of the framework, and on real human data to show its practical potential.

Index Terms— computational model, image-derived, meshfree, clinical data

1. INTRODUCTION

Recently modelling of patient-specific cardiac electrical activity has become an interesting research topic because the increasing attention to the model-based imaging technique of 3D cardiac electrical activity [1]. Currently the most popular computational model for modelling cardiac electrical activity is the reaction-diffusion model [2]. The reaction-diffusion model can reproduce a variety of physiological phenomena by introducing a large set of parameters to represent cardiac structure and cellular kinematics, but the simulation using reaction-diffusion model and complicated cellular model is still a challenge computational work [2]. Many numerical schemes have been applied to the reaction-diffusion model, including popular finite element methods (FEMs). Properly considering the geometrical complexity, the fiber structures and the material inhomogeneity, FEMs have produced fair results [3, 4]. However, mesh representation for the heart is a very complicated and time-consuming task in the FEMs, with additional needs for taking care of the boundary, material discontinuities and fiber structures. The emerging meshfree methods represent an object by distributing sufficient sam-

pling nodes within the space bounded by the object boundary surfaces, without the needs for mesh generation or complicated coordinate transformation. These properties are very attractive to large scale simulation of electrical propagation in different cardiac geometries.

Though large attentions are focused on polishing the existing models or establishing more realistic models, incorporating a computational model to analyze clinical data has begun to gain more attentions, especially from medical image community [5, 6]. However, there are a lot of issues that restrict the performance of popular computational models in clinical data. The main reasons are burdensome computation caused by the complexity of computational models, and formidable task to adjust too much parameters of model according to clinical data. There have been several works aimed to establish computational models for modelling cardiac electrical activity from clinical data, but these models are over simplified or need complicated volumetric meshes [7, 5].

In our implementation, Element-free Galerkin method (EFGM) [8] is applied to solve a modified Fitzhugh-Nagumo (FHN) model [3] in an image-derived geometry, which is segmented by 3D active region model (ARM) [9]. This FHN model is a simplified reaction-diffusion model and its ability has been well proved in reference [3]. Another advantage brought from EFGM is zero natural boundary condition can be handle by Galerkin weak form naturally, but to numerically solve Galerkin weak form with zero natural boundary condition by EFGM, sufficient samples should be arranged in the boundaries. Finally we would like to indicate that the computational model generated by our meshfree framework from image data, can be incorporated into our previous cardiac information recovery framework [10].

2. METHODOLOGY

2.1. Representation of cardiac geometry

In this paper, a method of simultaneous segmentation and motion recovery of the left ventricle from 3D image sequences is applied. This variational strategy extends ARM to 3D, where each ARM node spatiotemporally evolves under the influences of the internal and external forces towards apparent boundary and structures in the image. Based upon repre-

a	b	c₁	c₂	d	d_f	d_{cf}
0.13	0.013	0.26	0.1	1.0	4.0	1.0

Table 1. Parameter of FHN Model

sensation of cardiac geometry, the physically meaningful continuum biomechanical model of the myocardium is adopted to regularize the intrinsic behavior of the ARM, while node-dependent imaging data, the temporal consistent models of the tissue geometry and kinematics, and the statistical priors of the myocardial tissue distributions are used as driving forces. Fig.(1) shows the result of segmentation in one MRI slice and boundary of endo- and epicardium of canine left ventricle. Cardiac geometry, which are extracted from MRI images, are shown in Fig.(6) with fiber orientations. The density of the node distribution depends on the requirement on accuracy, and it can be easily refined through node addition or reduction.

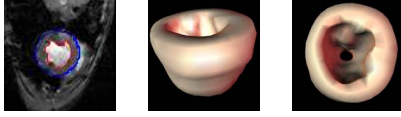


Fig. 1. From left to right: Segmentation result in one MRI image, the surface representation of the Left ventricle, front view and top view.

2.2. Galerkin weak form of FHN model

The differential equations of a modified FHN model [3] are:

$$\begin{aligned}
 \frac{\partial u}{\partial t} &= f(u, v) + \nabla \cdot (D \nabla u) \\
 \frac{\partial v}{\partial t} &= b(u - dv) \\
 f(u, v) &= c_1 u(u - a)(1 - u) - c_2 uv
 \end{aligned} \tag{1}$$

with natural boundary condition $\frac{\partial u}{\partial n} = 0$ since the heart is modeled as an isolated continuum. Parameter values are taken from [3] (table 1). State variable u is the excitation variable which corresponds to the transmembrane voltage, v is the recovery current variable, n is the normal of the boundary, $f(u, v)$ is the excitation term and a, b, c_1, c_2 and d are parameters that define the shape of action potential. These parameters are constant over time but not necessary in space. The change of state variables are determined by the excitation term $f(u, v)$ and diffusion term $\nabla \cdot (D \nabla u)$. If diffusion term is removed from FHN model the rest parts of FHN model can be considered as a microscopic cell model. Therefore, FHN model can be classified as one reaction-diffusion model [2]. Let U_I and V_I be the nodal values of field variables u and v at node x , and let Φ be the shape function constructed from moving least square (MLS) approximation, which will be stated in section 2.3. Then we have: $u \approx u^h = \Phi U_I, v \approx v^h = \Phi V_I$.

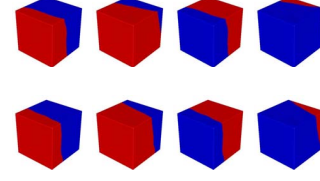


Fig. 2. From left to right propagation waves at 47ms, 95ms, 176ms, and 236ms with irregular sample nodes are shown (1106 nodes). Fiber orientation from top to down: (0.577, 0.577, -0.577); (0.577, -0.577, 0.577). 2^3 quadrature points in each background cell are applied in other columns. Red color represents active state and blue color represents quiescent state.

if u and v are placed with ΦU_I and ΦV_I respectively, continuous form of equation (1) can be written into a discrete Galerkin form, readers can refer to reference [11] for more details about transformation from equation (1) to (2):

$$\begin{aligned}
 \frac{\partial U_I}{\partial t} \int_{\Omega} \Phi^T \Phi d\Omega &= -U_I \int_{\Omega} (\nabla \Phi^T D_{tran} \nabla \Phi) d\Omega + \\
 &\quad f(U_I, V_I) \int_{\Omega} \Phi^T \Phi d\Omega \\
 \frac{\partial V_I}{\partial t} \int_{\Omega} \Phi^T \Phi d\Omega &= b(U_I - dV_I) \int_{\Omega} \Phi^T \Phi d\Omega
 \end{aligned} \tag{2}$$

where D_{tran} is the diffusion tensor transformed from local coordinate. D_{tran} of one point with α and β defining a rotation around the y - and z - axis of the global coordinate system according to the fiber orientation can be defined:

$$D_{tran} = A^{-1} D A, \quad A = R_{xz} R_{xy}$$

$$R_{xy} = \begin{bmatrix} \cos \alpha & \sin \alpha & 0 \\ -\sin \alpha & \cos \alpha & 0 \\ 0 & 0 & 1 \end{bmatrix}, \quad R_{xz} = \begin{bmatrix} \cos \beta & 0 & \sin \beta \\ 0 & 1 & 0 \\ -\sin \beta & 0 & \cos \beta \end{bmatrix}$$

and

$$D = \begin{bmatrix} d_f & 0 & 0 \\ 0 & d_{cf} & 0 \\ 0 & 0 & d_{cf} \end{bmatrix}$$

where d_f is the propagation speed along the fiber, and d_{cf} is the propagation speed cross the fiber.

2.3. MLS approximation

In our approach, moving-least squares (MLS) [12] method is used to construct the shape functions, since the function constructed from MLS approximation provides the desired order of consistency, and is smooth throughout the entire domain. In the MLS approximation the approximation $u^h(\mathbf{x})$ becomes

$$u^h(\mathbf{x}) = \sum_{I=1}^n \sum_{j=1}^m p_j(\mathbf{x}) (A^{-1}(\mathbf{x}) B(\mathbf{x}))_{jI} \tag{3}$$

$$= \sum_{I=1}^n \phi_I(\mathbf{x}) u_I = \Phi(\mathbf{x}) U \tag{4}$$

where

$$A(\mathbf{x}) = \sum_{I=1}^n w_I(x)p(x_I)p^T(x_I), w_I(x) \equiv w(x - x_I) \quad (5)$$

$$B(\mathbf{x}) = [w_1(x)p(x_1), w_2(x)p(x_2), \dots, w_n(x)p(x_n)] \quad (6)$$

$$U^T = [u_1, u_2, \dots, u_n] \quad (7)$$

In the above equations $w_I(x)$ is the cubic spline weight function, which is defined:

$$w(r) = \begin{cases} \frac{2}{3} - 4r^2 + 4r^3 & \text{for } r \leq \frac{1}{2} \\ \frac{4}{3} - 4r + 4r^2 - \frac{4}{3}r^3 & \text{for } \frac{1}{2} < r \leq 1 \\ 0 & \text{for } r > 1 \end{cases} \quad (8)$$

Let $r = \|x - x_I\|/d_{mI}$, where d_{mI} is the radius of the influence domain of a node. Rewrite equations (2) with matrices:

$$\begin{aligned} \frac{\partial U_I}{\partial t} &= M^{-1}KU_I + f(U_I, V_I) \\ \frac{\partial V_I}{\partial t} &= b(U_I - dV_I) \end{aligned} \quad (9)$$

$$f(U_I, V_I) = c_1 U_I(1 - U_I)(U_I - a) - c_2 U_I V_I$$

$$\begin{aligned} M_{i,j} &= \int_{\Omega} \phi_i^T \phi_j d\Omega, K_{i,j} = \int_{\Omega} B_i^T D_{tran} B_j d\Omega \\ B_i &= \begin{pmatrix} \phi_{i,x} \\ \phi_{i,y} \\ \phi_{i,z} \end{pmatrix} \end{aligned} \quad (10)$$

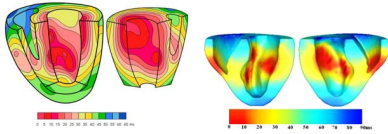


Fig. 3. Isochronic representation of ventricle activation. From left to right: published measurements, simulation of our meshfree framework

2.4. Integration schemes

In EFGM a regular background mesh, which consists of non-overlapping regular cells is required in performing the integration of Galerkin weak form. Therefore, a background mesh of proper density needs to be designed to approximate solutions of desired accuracy and handle natural boundary conditions correctly. In the regular-grid cell structures, there may exist cells that do not entirely belong to the problem domain. A simple visibility scheme that automatically separates the portion of the cell which lies outside of the physical domain is employed.

3. VALIDATIONS AND RESULTS

Synthetic geometry In order to assess the performances of EFGM, electrical propagations are first tested in a cube,

whose size is $60mm \times 60mm \times 60mm$. To find proper density of sample nodes to reach a stable speed of propagation wave, two series of isotropic electrical propagations with increasing regular sample nodes, but different quadrature points in the background cells, are solved in the cube by setting an initial potential, 0.5, on the nodes along one side of the cube. The converge curves are displayed in Fig.(4). From Fig.(4), we can see that the propagation speed starts to converge after nodes are more than 10^3 . Finally 1106 irregular sample nodes are places in the cube to generate plane wave by setting an initial potential in one side of the cube. The propagation is displayed in Fig.(2).

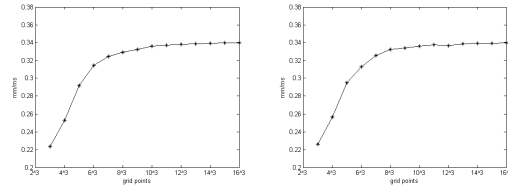


Fig. 4. The convergence of the speed of propagation wave with increasing density of regular sample nodes. (a) 2^3 quadrature points in each background cell; (b) 3^3 quadrature points in each background cell

Auckland heart model In order to assess the accuracy and efficiency of our meshfree framework, electrical propagation in auckland heart model¹ are solved with known diffusion tensors and purkinje network extremities. Since such measurement data of purkinje network is not available yet, we have to define those extremities manually. From Fig.(3), the figure generated from Durrer's [13] measurements from isolated human hearts, we can see that purkinje network extremities are located on the endocardium and then we define similar locations of extremities in auckland cardiac geometry by hand. Simulation of our meshfree framework in auckland heart model is also displayed in Fig.(3). Since it is reported that isolation of the heart leads to an increase in conduction velocity [13] and durations of QRS waveform in healthy individuals vary from 70ms to 80ms the activation process in our simulation are qualitatively close to the published measurements as we can see in Fig.(3). We also projected our propagations into body surface to generate surface potentials and result is display in Fig.(3), too. We also simulate one case of heart disease, Right bundle branch block (RBBB) and its BSPs on the torso surface, which are compared to normal TMPs and BSPs in Fig.(5). In this comparison the differences between normal case and diseased case have shown the ability of our framework in reproducing different phenomena of cardiac electrophysiological activities.

Left ventricular geometry Since patient-specific geometries of human hearts are unavailable for the moment,

¹<http://www.bioeng.auckland.ac.nz/cmiss/cmiss.php>

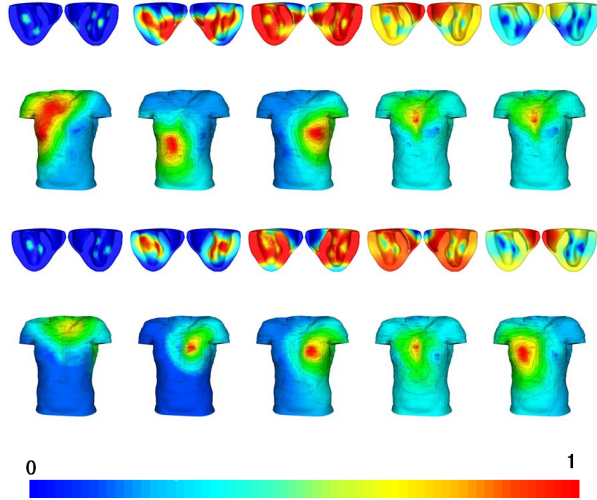


Fig. 5. Five samples of normal TMPs and BSPs during one cardiac cycle: (a) transmembrane potentials in the heart, (b) BSPs on the torso surface. Five samples of TMPs and BSPs during one cardiac cycle under the condition of RBBB: (c) transmembrane potentials in the heart, (d) BSPs on the torso surface. All the potentials are normalized between 0 and 1 and displayed according to color mapping bar.

a left ventricle of the canine heart segmented by 3D ARM [9], is used for the simulation of electrical propagation in this paper. Purkinje network extremities are manually placed according to Durrer's measurement [13], too. Fiber orientations of the left ventricle of canine heart are obtained by mapping the data from auckland heart model with the iterative closest points algorithm [14]. Fiber orientations and electrical propagation on left ventricular geometry are shown in Fig.(6) respectively.

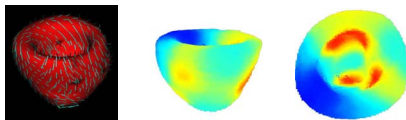


Fig. 6. From left to right: Fiber structure, front view and top view of simulation on left ventricle

4. CONCLUSION

We have presented a meshfree framework for building a computational model from an image-derived geometry. Validations in Auckland heart model has demonstrated the ability of our meshfree framework in providing a physiological meaningful and computational feasible model for simulations and our recovery frameworks. We also show our framework's po-

tential in the left ventricle, but in the near future, we should explore our framework's ability in the whole heart.

5. REFERENCES

- [1] L.W. Wang, H.Y. Zhang, C.L. Ken Wong, H.F. Liu, and P.C. Shi, "Noninvasive imaging of 3D cardiac electrophysiology," in *ISBI*, 2007, pp. 632–635.
- [2] A.J. Pullan, M.L. Buist, and L.K. Cheng, *Mathematically modelling the electrical activity of the heart : from cell to body surface and back again*, World Science Publishing Co. Pte. Ltd, Singapore, 2005.
- [3] Rogers J.M. and McCulloch A.D., "A collation-galerkin finite element model of cardiac action potential propagation.," *IEEE Trans. Biomed. Eng.*, vol. 41, no. 8, pp. 743–756, 1994.
- [4] Smith N.P. Clark K. Mulquiney, P.J. and P.J. Hunter, "Mathematical modelling of the ischaemic heart," *Nonlinear Analysis*, vol. 47, pp. 235–244, 2001.
- [5] M. Sermesant, H. Delingette, and N. Ayache, "An electromechanical model of the heart for image analysis and simulation.," *IEEE Trans. Med. Imaging*, vol. 25, no. 5, pp. 612–625, 2006.
- [6] C. L. ken Wong, L.W. Wang, H.Y. Zhang, H.F. Liu, and P.C. Shi, "Integrating functional and structural images for simultaneous cardiac segmentation and deformation recovery," in *MICCAI*, 2007, pp. 270–277.
- [7] M. Sermesant, Y. Coudière, V. Moreau-Villéger, K.S. Rhode, D.L.G. Hill, and R.S. Razavi, "A fast-marching approach to cardiac electrophysiology simulation for XMR interventional imaging," in *MICCAI*, 2005, pp. 607 – 615.
- [8] Belystchko T., Lu Y.Y. and Gu L., "Element-free galerkin methods," *Int. J. Numer. Methods Eng.*, vol. 37, pp. 229–256, 1994.
- [9] L. Zhuang, H.F. Liu, H.J. Chen, W. abd Bao, and P.C. Shi, "Simultaneous segmentation and motion recovery in 3D cardiac image analysis," in *CVBIA*, 2005, pp. 499–507.
- [10] L.W. Wang, H.Y. Zhang, P.C. Shi, and H.F. Liu, "Imaging of 3D cardiac electrical activity: A model-based recovery framework," in *MICCAI*, 2006, pp. 792–799.
- [11] P.C. Shi H.Y. Zhang, L.W. Wang, "Simulations of cardiac electrophysiological activities using a heart-torso model," in *FIMH*, 2007, pp. 150–159.
- [12] Lancaster P. and Salkauskas, "Surface generated by moving least squares methods.," *Math. Comp.*, vol. 37, no. 155, pp. 141–158, 1982.
- [13] G. Freud M. Janse F. Meijler D. Durrer, R. van Dam and R. Arzbaecher, "Total excitation of the isolated human heart," *Circulation*, vol. 41, no. 6, pp. 899–912, 1970.
- [14] P. Besl and H. McKay, "A method for registration of 3D shapes.," *IEEE Trans. Pattern. Anal.*, vol. 14, no. 155, pp. 239–256, 1992.